

# Carbon nanotubes as photoacoustic molecular imaging agents in living mice

ADAM DE LA ZERDA<sup>1,2</sup>, CRISTINA ZAVALA<sup>1</sup>, SHAY KEREN<sup>1</sup>, SRIKANT VAITHILINGAM<sup>2</sup>, SUNIL BODAPATI<sup>1</sup>, ZHUANG LIU<sup>3</sup>, JELENA LEVI<sup>1</sup>, BRYAN R. SMITH<sup>1</sup>, TE-JEN MA<sup>2</sup>, OMER ORALKAN<sup>2</sup>, ZHEN CHENG<sup>1</sup>, XIAOYUAN CHEN<sup>1</sup>, HONGJIE DAI<sup>3</sup>, BUTRUS T. KHURI-YAKUB<sup>2</sup> AND SANJIV S. GAMBHIR<sup>1,4\*</sup>

<sup>1</sup>Molecular Imaging Program at Stanford, Department of Radiology and Bio-X Program, Stanford University, Palo Alto, California 94305, USA

<sup>2</sup>Department of Electrical Engineering, Stanford University, Palo Alto, California 94305, USA

<sup>3</sup>Department of Chemistry, Stanford University, Palo Alto, California 94305, USA

<sup>4</sup>Department of Bioengineering, Stanford University, Palo Alto, California 94305, USA

\*e-mail: sgambhir@stanford.edu

Published online: 17 August 2008; doi:10.1038/nnano.2008.231

Photoacoustic imaging of living subjects offers higher spatial resolution and allows deeper tissues to be imaged compared with most optical imaging techniques<sup>1–7</sup>. As many diseases do not exhibit a natural photoacoustic contrast, especially in their early stages, it is necessary to administer a photoacoustic contrast agent. A number of contrast agents for photoacoustic imaging have been suggested previously<sup>8–15</sup>, but most were not shown to target a diseased site in living subjects. Here we show that single-walled carbon nanotubes conjugated with cyclic Arg-Gly-Asp (RGD) peptides can be used as a contrast agent for photoacoustic imaging of tumours. Intravenous administration of these targeted nanotubes to mice bearing tumours showed eight times greater photoacoustic signal in the tumour than mice injected with non-targeted nanotubes. These results were verified *ex vivo* using Raman microscopy. Photoacoustic imaging of targeted single-walled carbon nanotubes may contribute to non-invasive cancer imaging and monitoring of nanotherapeutics in living subjects<sup>16</sup>.

Recently, we reported on the conjugation of cyclic RGD containing peptides to single-walled carbon nanotubes<sup>17</sup> (SWNT–RGD) that is stable in serum. The single-walled carbon nanotubes, which were 1–2 nm in diameter and 50–300 nm in length were coupled to the RGD peptides through polyethylene glycol-5000 grafted phospholipid (PL–PEG<sub>5000</sub>). These SWNT–RGD conjugates bind with high affinity to  $\alpha_v\beta_3$  integrin, which is over-expressed in tumour neovasculature, and to other integrins expressed by tumours but with lower affinity<sup>18,19</sup>. We also synthesized non-targeted single-walled carbon nanotubes (that is, plain single-walled carbon nanotubes) by conjugating them solely to PL–PEG<sub>5000</sub> (Fig. 1a). Our photoacoustic instrument<sup>20</sup> used a single-element focused transducer to raster scan the object under study, which was illuminated through a fibre head (see Methods and Supplementary Information, Fig. S1). In a phantom study we measured the photoacoustic signal of plain single-walled carbon nanotubes and SWNT–RGD at wavelengths of 690–800 nm (Fig. 1b; shorter wavelengths are less desirable as the depth of penetration through the tissues is reduced<sup>21</sup>). These photoacoustic spectra suggest that 690 nm is

the preferable wavelength, because the photoacoustic signal of the single-walled carbon nanotubes is highest at that wavelength. Furthermore, the ratio of single-walled carbon nanotubes to haemoglobin signal is higher at this wavelength when compared with other wavelengths. Importantly, the photoacoustic signal of single-walled carbon nanotubes was found to be unaffected by the RGD peptide conjugation. This finding was validated through measurements of the optical absorbance of the two single-walled carbon nanotubes conjugates (see Supplementary Information, Fig. S2). In a separate non-absorbing and non-scattering phantom study, we also validated that the photoacoustic signal produced by single-walled carbon nanotubes is in linear relationship with their concentration (Fig. 1c) with  $R^2 = 0.9997$ .

We then subcutaneously injected the lower back of a mouse with 30  $\mu$ l of mixtures of single-walled carbon nanotubes and matrigel at concentrations between 50 and 600 nM ( $n = 3$  for each concentration). Matrigel alone produced no photoacoustic signal (data not shown). Upon injection, the matrigel solidified, fixing the single-walled carbon nanotubes in place. Three-dimensional (3D) ultrasound and photoacoustic images of the inclusions were then acquired (Fig. 2a). The ultrasound images showed the mouse anatomy (for example, skin and inclusion edges), and the photoacoustic images revealed the single-walled carbon nanotubes contrast in the mouse. The photoacoustic signal from each inclusion was quantified using a 3D region of interest drawn over the inclusion. We observed a linear correlation ( $R^2 = 0.9929$ ) between the single-walled carbon nanotubes concentration and the corresponding photoacoustic signal (Fig. 2b). Importantly, this linear relation can only be expected in special cases where the dye concentration does not perturb the tissue light distribution significantly. We concluded that the photoacoustic signal produced by tissues (background) was equivalent to the photoacoustic signal produced by 50 nM of single-walled carbon nanotubes (that is, a signal-to-background ratio of 1). This experimental result correlates well with the theoretical analysis (see Supplementary Information), which predicts a background signal equal to 7–70 nM of single-walled carbon nanotubes, depending on the location of the nanotubes in the body.

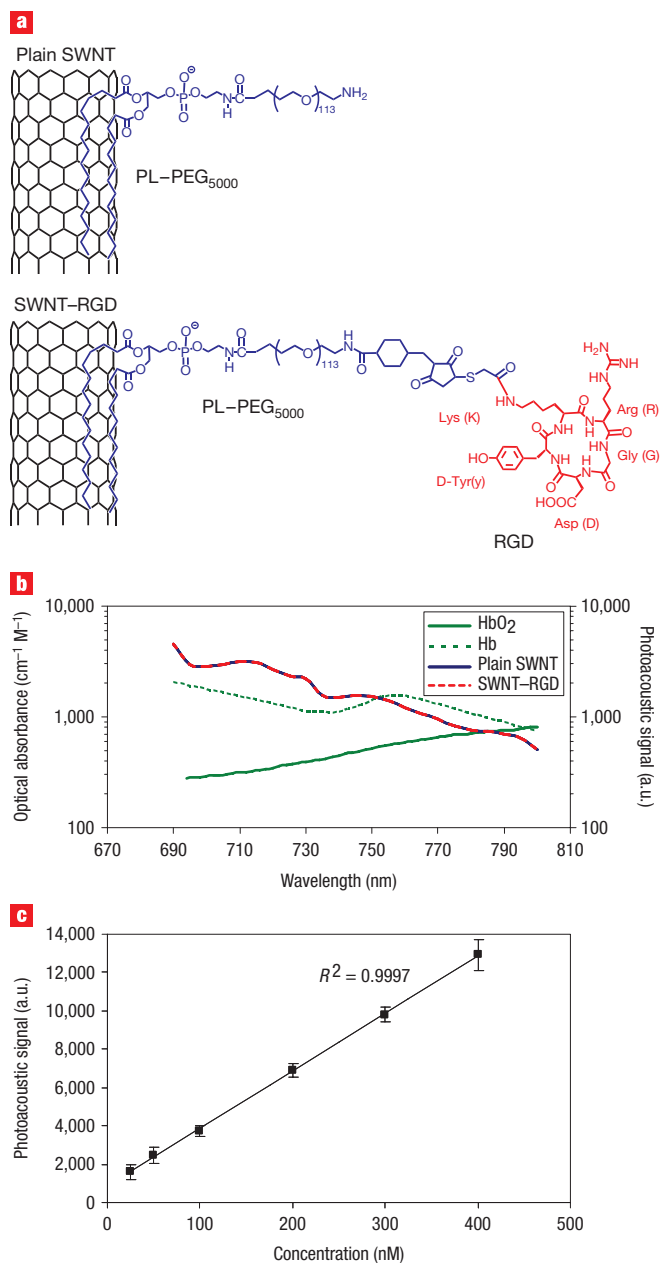


**Figure 1** Characterization of the photoacoustic properties of single-walled carbon nanotubes. **a**, Illustration of plain single-walled carbon nanotubes (plain SWNT) and SWNT-RGD. The phospholipid binds to the sidewall of the single-walled carbon nanotubes connecting the PEG<sub>5000</sub> to the nanotubes. The RGD allows the single-walled carbon nanotubes to bind to tumour integrins such as  $\alpha_v\beta_3$ . **b**, The photoacoustic spectra of plain single-walled carbon nanotubes and SWNT-RGD are overlaid on the known optical absorbance of HbO<sub>2</sub> and Hb. The spectral overlap between plain single-walled carbon nanotubes and SWNT-RGD suggests that the RGD conjugation does not perturb the photoacoustic signal. **c**, The photoacoustic signal produced by single-walled carbon nanotubes was observed to be linearly dependent on the concentration ( $R^2 = 0.9997$ ).

We then injected two groups of mice bearing U87MG tumour xenografts ( $\sim 100$  mm<sup>3</sup>) through the tail-vein (IV) with either 200  $\mu$ l of plain single-walled carbon nanotubes ( $n = 4$ ) or SWNT-RGD ( $n = 4$ ) at a concentration of 1.2  $\mu$ M.

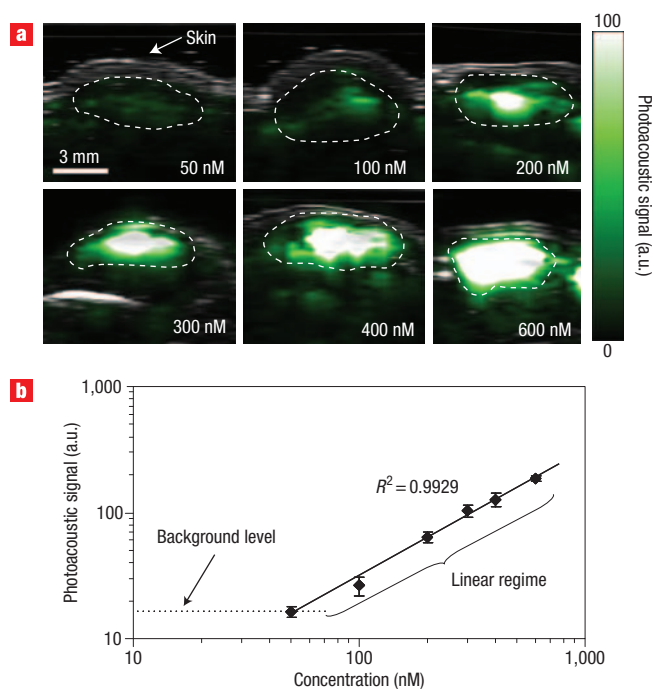


**Figure 2** Photoacoustic detection of single-walled carbon nanotubes in living mice. **a**, Mice were injected subcutaneously with single-walled carbon nanotubes at concentrations of 50–600 nM. One vertical slice in the 3D photoacoustic image (green) was overlaid on the corresponding slice in the ultrasound image (grey). The skin is visible in the ultrasound images, and the photoacoustic images show the single-walled carbon nanotubes. The dotted lines on the images identify the edges of each inclusion. **b**, The photoacoustic signal from each inclusion was calculated. The background level represents the endogenous signal measured from tissues. The error bars represent standard error ( $n = 3$ ). The linear regression is calculated on the five most concentrated inclusions ( $R^2 = 0.9929$ ).

Three-dimensional ultrasound and photoacoustic images of the tumour and its surroundings were acquired before and up to 4 h after injection. We found that mice injected with SWNT-RGD showed a significant increase of photoacoustic signal in the tumour compared with control mice injected with plain single-walled carbon nanotubes (Fig. 3a). The images from the different time points were aligned with one another using simple vertical translations to account for small vertical movements in the transducer positioning. This alignment allowed quantification of the photoacoustic signal at all time points using a single region of interest. We then calculated a subtraction image between the photoacoustic image taken at 4 h post-injection and the photoacoustic image taken before injection. The subtraction image better visualizes the real distribution of the single-walled carbon nanotubes as it removes, to a large extent, the background signal. For example, in the mouse injected with plain single-walled carbon nanotubes (Fig. 3a), a high photoacoustic signal, likely produced by a large blood vessel, was seen in the pre-injection and post-injection images. However, the subtraction image showed a much lower signal from this area, reflecting the likely low concentration of plain single-walled carbon nanotubes there. We calculated the photoacoustic signal by drawing a 3D region of interest around the tumour (tumour boundaries were clearly visualized in the ultrasound images). The photoacoustic signal increase was quantified as a function of time

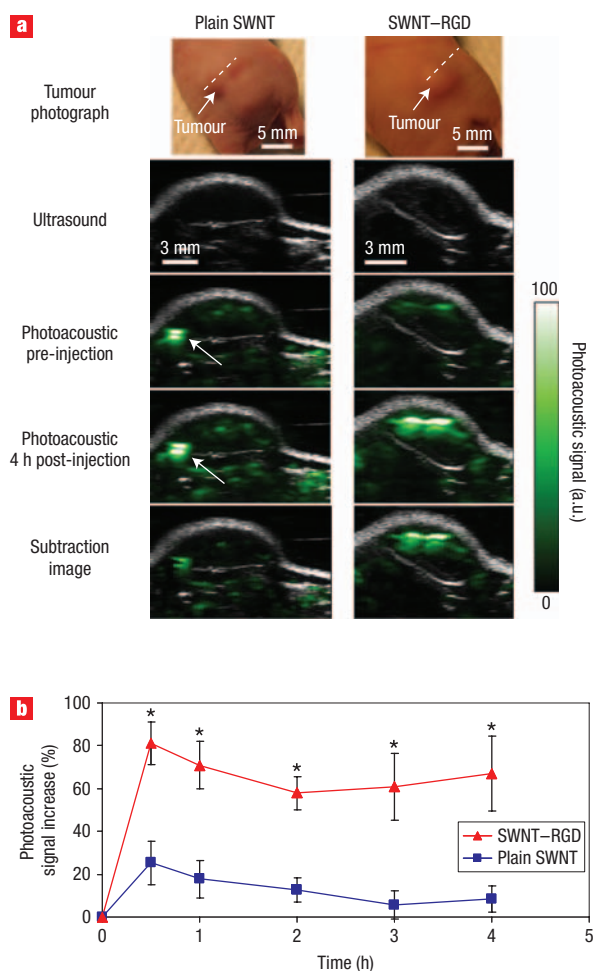


**Figure 3** Single-walled carbon nanotube targets tumour in living mice.

**a**, Ultrasound (grey) and photoacoustic (green) images of one vertical slice (white dotted line) through the tumour. The ultrasound images show the skin and tumour boundaries. Subtraction images were calculated as the 4 h post-injection image minus the pre-injection image. The high photoacoustic signal in the mouse injected with plain single-walled carbon nanotubes (indicated with a white arrow) is not seen in the subtraction image, suggesting that it is due to a large blood vessel and not single-walled carbon nanotubes. **b**, Mice injected with SWNT-RGD showed a significantly higher photoacoustic signal than mice injected with plain single-walled carbon nanotubes ( $P < 0.001$ ). The error bars represent standard error ( $n = 4$ ).  $*P < 0.05$ .

(Fig. 3b). Although SWNT-RGD led to a consistently higher photoacoustic signal, plain single-walled carbon nanotubes led only to a temporary increase in the photoacoustic signal of the tumour ( $P < 0.001$  when comparing entire time-curves, and  $P < 0.05$  when comparing the signals at each time point independently). The temporary photoacoustic signal observed for plain single-walled carbon nanotubes is likely caused by circulating nanotubes that are eventually cleared from the bloodstream. Conversely, SWNT-RGD bind to the tumour vasculature, creating a consistent photoacoustic signal from the tumour. On average, at 4 h post-injection, the SWNT-RGD resulted in  $\sim 8$  times greater increase in photoacoustic signal compared with plain single-walled carbon nanotubes. The percentage injected dose per gram of tissue was calculated to be  $\sim 14$  %ID  $g^{-1}$  (see Supplementary Information).

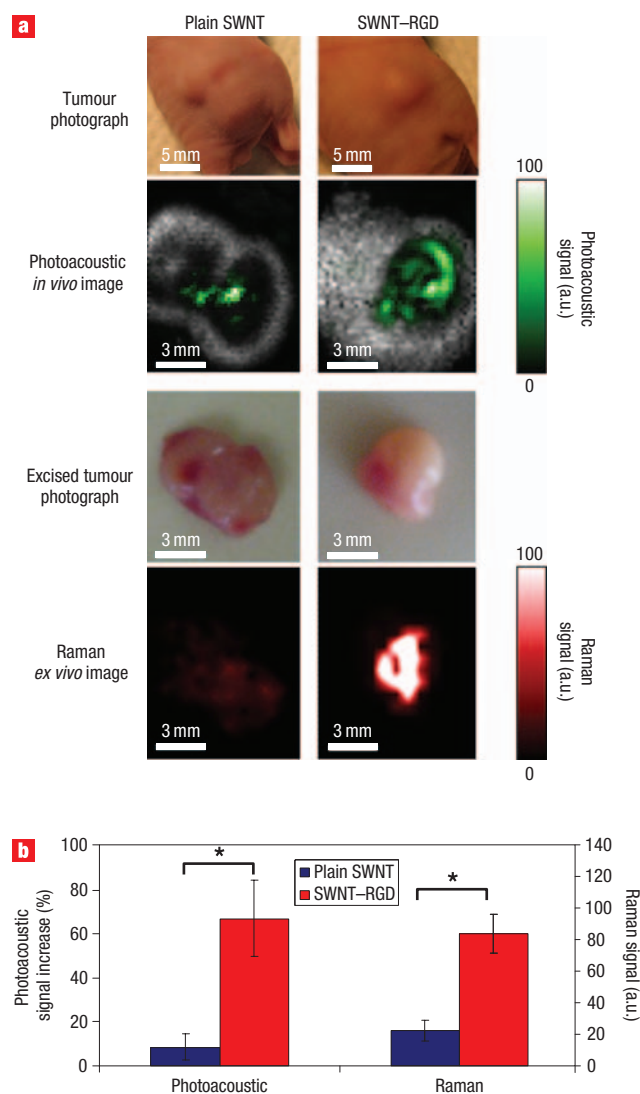


**Figure 4** Validation of the *in vivo* photoacoustic images by Raman *ex vivo* microscopy.

**a**, Photographs of the tumours in mice and the corresponding photoacoustic subtraction images (green) shown as horizontal slices through the tumours. After the photoacoustic scan, the tumours were excised and scanned using a Raman microscope (red). Mice injected with plain single-walled carbon nanotubes (left-hand column) showed both low photoacoustic and Raman signals compared with mice injected with SWNT-RGD (right-hand column). The tumours are in the same orientation in all images. **b**, Comparison between the photoacoustic signal of the tumours *in vivo* (left) and the Raman signal acquired from the excised tumours (right).  $*P < 0.05$ .

We further validated our photoacoustic results using a Raman microscope, as an independent method for detection of single-walled carbon nanotubes. At the conclusion of the photoacoustic study, 4 h post-injection, the mice were sacrificed; the tumours were surgically removed and scanned *ex vivo* under a Raman microscope. The two-dimensional Raman images of the excised tumours were found to match the photoacoustic images (Fig. 4a). The mean Raman signal from the tumours was calculated from the Raman images. Similarly to the photoacoustic results, the Raman signal from the tumours was  $\sim 4$  times higher in mice injected with SWNT-RGD than in mice injected with plain single-walled carbon nanotubes (Fig. 4b).

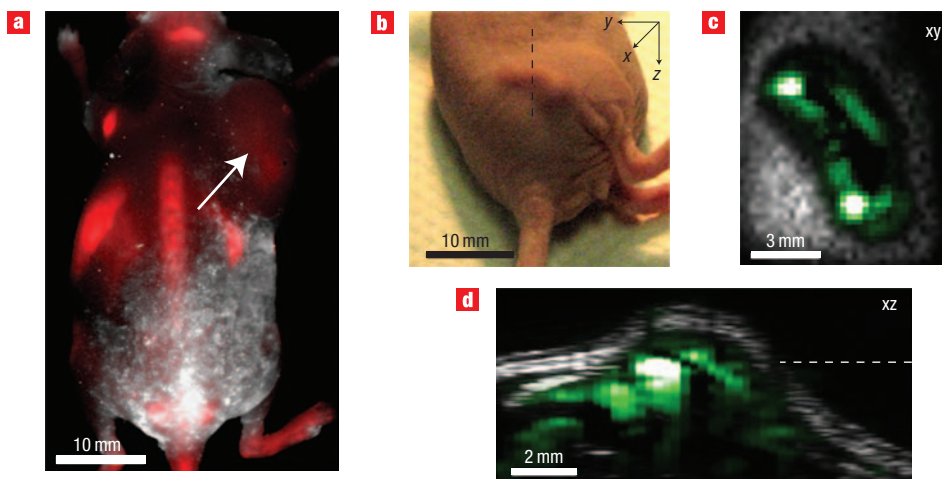


**Figure 5** Comparison between photoacoustic imaging using single-walled carbon nanotubes and fluorescence imaging using quantum dots.

**a**, Fluorescence image (red) of a mouse injected with QD–RGD. The white arrow indicates the tumour location. The other bright spots on the image represent the different organs in which QD–RGD non-specifically accumulated. **b**, Tumor photograph. **c**, Horizontal ( $xy$  plane) and **d**, vertical ( $xz$  plane) slices in the 3D photoacoustic image of a mouse injected with SWNT–RGD. The black dotted line shows the vertical slice orientation and the white dotted line shows the height of the horizontal slice in the vertical slice. The location of the single-walled carbon nanotubes in the tumour is visualized with high spatial resolution.

Unlike photoacoustic imaging, optical imaging suffers from relatively poor spatial resolution as well as exponentially degraded sensitivity as tissue depth increases<sup>22</sup>. We showed the superiority of our photoacoustic strategy by comparing it with fluorescence imaging of tumour-targeted quantum dots. The quantum dots were conjugated to RGD peptides<sup>23</sup> (QD–RGD) and imaged 6 h post-injection using a fluorescence imaging instrument (Fig. 5a). Although the quantum dot and single-walled carbon nanotube conjugates might have different biodistributions, the photoacoustic images of single-walled carbon nanotubes from the tumour illustrated the depth-information and the greater spatial resolution achieved by photoacoustic imaging compared with fluorescence imaging (Fig. 5b–d). The smeared signal from the tumour in the fluorescence image is due to light scattering. However, the photoacoustic images showed the 3D distribution of SWNT–RGD in the tumour with high spatial resolution. Similar results were also observed in a phantom study (see Supplementary Information, Fig. S4).

We have demonstrated that single-walled carbon nanotubes can be exploited as photoacoustic contrast agents to non-invasively image tumours. Intravenous injection of targeted single-walled carbon nanotubes in mice led to 8 times higher photoacoustic signal in the tumour compared with mice injected with non-targeted single-walled carbon nanotubes. Our photoacoustic images were verified using Raman microscopy on the surgically removed tumours. Furthermore, our results agreed with a previous study<sup>17</sup> where radiolabelled SWNT–RGD were monitored using small animal positron emission tomography (microPET). In that study SWNT–RGD were found to accumulate  $\sim 3$ – $5$  times more in tumours than plain single-walled carbon nanotubes. That study also showed that the SWNT–RGD did not accumulate in the tissue surrounding the tumour.

Most previous work on photoacoustic contrast agents *in vivo* is limited to non-targeted agents such as gold nanocages used for highlighting the blood vessels in a rat's brain<sup>11</sup>. A recent preliminary study<sup>13</sup> showed that an indocyanine green derivative (IRDye-800-c(KRGDf)) may be applicable for photoacoustic

spectroscopic imaging of U87MG tumours; however, the study was carried out on a single mouse and statistical validation of the agent has yet to be shown. Various gold nanoparticles have been previously suggested, primarily for their high absorption characteristics and the ability to control their spectra, which allows multiplexing studies<sup>9</sup>. However, their main limitation is their relatively large size, which will lead to their rapid clearance by the reticuloendothelial system (RES) upon intravenous injection. It is possible that single-walled carbon nanotubes, due to their unique high aspect ratio ( $\sim 1:100$ ) and high surface area to volume ratio, are capable of minimizing RES uptake while having an increased affinity for molecular targets due to multivalency effects<sup>17</sup>. A concentration of 50 nM of single-walled carbon nanotubes was found to produce a photoacoustic signal equivalent to mouse tissues (background); however, the minimum detectable concentration of single-walled carbon nanotubes is likely to be less than 50 nM. This is because photoacoustic images were acquired before and after the administration of the contrast agent, thus making it possible to separate the contrast agent signal from the background signal. Further background reduction can be achieved by performing photoacoustic spectral imaging, improving hardware/reconstruction software, or by enhancing the single-walled carbon nanotubes' photoacoustic signal. With respect to acquisition time, our current instrument acquires a single photoacoustic image in  $\sim 20$ – $30$  minutes for a tumour  $\sim 100$  mm<sup>3</sup> in size. However, by using lasers with higher repetition rates, scan duration can be greatly reduced.

We are currently investigating the potential of single-walled carbon nanotubes to extravasate out of the leaky vasculature of tumours. Single-walled carbon nanotube extravasation is of particular interest, because upon exiting the vasculature, the nanotubes would have access to many more molecular targets that exist only on the cancer cell's membranes. Future work should optimize the particles' extravasation as well as bring new technologies to help quantify the degree of nanotube extravasation. Moreover, future studies can monitor various nano-therapeutic applications such as drug-eluting single-walled

carbon nanotubes using photoacoustic imaging. Such nano-therapeutic and cancer imaging applications would gain further clinical interest as single-walled carbon nanotubes continue to show no toxic effects<sup>24</sup>. Although single-walled carbon nanotubes have the capability to efficiently bind to molecular targets, their high photoacoustic signal allows for high-resolution 3D photoacoustic images with substantial depth of penetration. None of the other molecular imaging modalities compares with the precise depth information and submillimetre resolution at nanomolar sensitivity that is achieved by photoacoustic imaging. We expect this work to stimulate further studies of biologically relevant problems using photoacoustic molecular imaging.

## METHODS

### SYNTHESIS OF SINGLE-WALLED CARBON NANOTUBE CONJUGATES

A complete description of the synthesis of SWNT-RGD and plain single-walled carbon nanotubes can be found elsewhere<sup>17</sup>. The single-walled carbon nanotubes used in this work were 50–300 nm in length and 1–2 nm in diameter. The molar concentrations<sup>25</sup> were based on an average molecular weight of 170 kDa per single-walled carbon nanotube (150 nm in length and 1.2 nm in diameter).

### STATISTICAL METHODS

For the single-walled carbon nanotube tumour targeting experiments, we used a random-effects regression to test the hypothesis that mice injected with SWNT-RGD showed an increased photoacoustic signal over time in the tumour compared with the control group injected with plain single-walled carbon nanotubes. We also performed the one-tailed student's *t*-test at each time point independently to test whether the previous effect will be observed by sampling the photoacoustic signal at a single time point instead. For the cell uptake studies, we used the one-tailed student's *t*-test to test whether the group in which U87MG cells were exposed to SWNT-RGD had a statistically higher signal than each of the other groups independently.

### PHOTOACOUSTIC INSTRUMENTATION

Our in-house photoacoustic system<sup>20</sup> is illustrated in the Supplementary Information, Fig. S1. A tuneable pulsed laser with a repetition rate of 10 Hz and a pulsewidth of 5 ns (Nd:YAG Surelight-III-10 connected to Surelite OPO Plus, Continuum) illuminated the object through a fibre-optic ring light (50-1353 Ringlight, Fiberoptic Systems). The average energy density of the laser at 690 nm wavelength was measured to be  $\sim 9$  mJ cm<sup>-2</sup> at the target site, which is below the ANSI limitation for laser skin exposure<sup>26</sup>. A 5 MHz focused transducer (25.5 mm focal length, 4 MHz bandwidth, F number of 2.0, depth of focus of 6.5 mm, lateral resolution of 600  $\mu$ m and axial resolution of 380  $\mu$ m; A309S-SU-F-24.5-MM-PTE, Panametrics) was used to acquire both pulse-echo and photoacoustic images. In addition, high-resolution ultrasound images were acquired using a 25 MHz focused transducer (27 mm focal length, 12 MHz bandwidth, F number of 4.2, depth of focus of 7.5 mm, lateral resolution of 250  $\mu$ m and axial resolution of 124  $\mu$ m; V324-SU-25.5-MM, Panametrics). A precision xyz-stage (U500, Aerotech) with minimum step size of 1  $\mu$ m was used to move the transducer and the fibre ring along a planar 2D trajectory. At every position, the acquired signal was averaged over 16 laser pulses. The time of arrival and the intensity of the laser pulses were recorded using a silicon photodiode (DET10A, Thorlabs). This information was used to synchronize the acquisition and compensate for pulse-to-pulse variations in laser intensity. The analogue photoacoustic signals were amplified using a 40 dB preamplifier (5676/115VAC, Panametrics) and digitized using an oscilloscope (Infinium 54825A, Agilent). The photoacoustic and ultrasound images were reconstructed as follows: the a-scan from each position of the transducer was bandpass-filtered with 100% fractional bandwidth, compensated for laser intensity variation and envelope detected. The a-scans were then combined to reconstruct a 3D intensity image of the target. No further post-processing was carried out on the images. The ultrasound images acquired using the 5 MHz and 25 MHz transducers were aligned together using small vertical translations so that the object's skin level matched in both images. The photoacoustic and high-frequency ultrasound images were analysed, co-registered, and displayed using AMIDE<sup>27</sup> software.

### SINGLE-WALLED CARBON NANOTUBE TUMOUR TARGETING IN LIVING MICE

All animal experiments were performed in compliance with the Guidelines for the Care and Use of Research Animals established by the Stanford University

Animal Studies Committee. Two groups of female nude mice ( $n = 3$  in each group), 6–8 weeks old were inoculated subcutaneously at their lower right back with 10<sup>7</sup> U87MG cells (American Type Culture Collection, ATCC) suspended in 50  $\mu$ l of saline (PBS, pH 7.4  $1 \times$ , Invitrogen). The tumours were allowed to grow to a volume of  $\sim 100$  mm<sup>3</sup>. Before the injection of single-walled carbon nanotubes, photoacoustic and ultrasound images of the mice were taken. Photoacoustic excitation light was 690 nm. The single-walled carbon nanotubes were sonicated for 5 min under 1 W r.m.s. (Sonifier 150, Branson) to separate single-walled carbon nanotubes that may have aggregated. The mice were then injected with 200  $\mu$ l of 1.2  $\mu$ M single-walled carbon nanotubes into the tail-vein. During the injection the positioning of the mice was not changed. After injection, photoacoustic and ultrasound images were acquired at 0.5, 1, 2, 3 and 4 h post injection. The scanning area varied between mice depending on the tumour orientation, but typically was  $\sim 80$  mm<sup>2</sup>, with a step size of 0.25 mm. At 4 h post-injection, the mice were killed and their tumours surgically removed for further *ex vivo* analysis. The ultrasound images from the different time points were aligned with one another by vertically translating the images (translation was typically less than 0.5 mm). The same alignment was then applied to the photoacoustic images. Using AMIDE software, a 3D region of interest was drawn over the tumour volume (which was clearly illustrated in the ultrasound images). The mean photoacoustic signal in the tumour region of interest was calculated for each photoacoustic image.

Received 10 December 2007; accepted 4 July 2008; published 17 August 2008.

### References

- Xu, M. H. & Wang, L. H. V. Photoacoustic imaging in biomedicine. *Rev. Sci. Instrum.* **77**, 041101 (2006).
- Oh, J. T. *et al.* Three-dimensional imaging of skin melanoma *in vivo* by dual-wavelength photoacoustic microscopy. *J. Biomed. Opt.* **11**, 34032 (2006).
- Zhang, H. F., Maslov, K., Stoica, G. & Wang, L. V. Imaging acute thermal burns by photoacoustic microscopy. *J. Biomed. Opt.* **11**, 054033 (2006).
- Wang, X., Xie, X., Ku, G., Wang, L. V. & Stoica, G. Noninvasive imaging of haemoglobin concentration and oxygenation in the rat brain using high-resolution photoacoustic tomography. *J. Biomed. Opt.* **11**, 024015 (2006).
- Zhang, H. F., Maslov, K., Stoica, G. & Wang, L. V. Functional photoacoustic microscopy for high-resolution and noninvasive *in vivo* imaging. *Nat. Biotechnol.* **24**, 848–851 (2006).
- Manohar, S. *et al.* Initial results of *in vivo* non-invasive cancer imaging in the human breast using near-infrared photoacoustics. *Opt. Express* **15**, 12277–12285 (2007).
- Ermilov, S. *et al.* Detection and noninvasive diagnostics of breast cancer with 2-colour laser optoacoustic imaging system. *Proc. SPIE* **6437**, 643703 (2007).
- Eghtedari, M. *et al.* High sensitivity of *in vivo* detection of gold nanorods using a laser optoacoustic imaging system. *Nano Lett.* **7**, 1914–1918 (2007).
- Li, P. C. *et al.* Photoacoustic imaging of multiple targets using gold nanorods. *IEEE Trans. Ultrason. Ferroelectr. Freq. Control* **54**, 1642–1647 (2007).
- Kim, G. *et al.* Indocyanine-green-embedded PEBBLES as a contrast agent for photoacoustic imaging. *J. Biomed. Opt.* **12**, 044020 (2007).
- Yang, X., Skrabalak, S. E., Li, Z. Y., Xia, Y. & Wang, L. V. Photoacoustic tomography of a rat cerebral cortex *in vivo* with Au nanocages as an optical contrast agent. *Nano Lett.* **7**, 3798–3802 (2007).
- Zharov, V. P. *et al.* Photoacoustic flow cytometry: principle and application for real-time detection of circulating single nanoparticles, pathogens and contrast dyes *in vivo*. *J. Biomed. Opt.* **12**, 051503 (2007).
- Li, M.-L. *et al.* Simultaneous molecular and hypoxia imaging of brain tumours *in vivo* using spectroscopic photoacoustic tomography. *Proc. IEEE* **96**, 481–489 (2008).
- Wei, C.-W. *et al.* *In vivo* photoacoustic imaging with multiple selective targeting using bioconjugated gold nanorods. *Proc. SPIE* **6856**, 68560J (2008).
- Kim, K. *et al.* *In vivo* imaging of inflammatory responses by photoacoustics using cell-targeted gold nanorods (GNR) as contrast agent. *Proc. SPIE* **6856**, 68560H (2008).
- Bianco, A., Kostarelos, K. & Prato, M. Applications of carbon nanotubes in drug delivery. *Curr. Opin. Chem. Biol.* **9**, 674–679 (2005).
- Liu, Z. *et al.* *In vivo* biodistribution and highly efficient tumour targeting of carbon nanotubes in mice. *Nature Nanotech.* **2**, 47–52 (2007).
- Mizejewski, G. J. Role of integrins in cancer: survey of expression patterns. *Proc. Soc. Exp. Biol. Med.* **222**, 124–138 (1999).
- Janssen, M. L. *et al.* Tumour targeting with radiolabelled alpha(v)beta(3) integrin binding peptides in a nude mouse model. *Cancer Res.* **62**, 6146–6151 (2002).
- Vaithilingam, S. *et al.* *Ultrasonics Symposium*, 2007, 2413–2416 (2007).
- Weissleder, R. & Ntziachristos, V. Shedding light onto live molecular targets. *Nature Med.* **9**, 123–128 (2003).
- Keren, S., Gheysens, O., Levin, C. S. & Gambhir, S. S. A comparison between a time domain and continuous wave small animal optical imaging system. *IEEE Trans. Med. Imaging* **27**, 58–63 (2008).
- Cai, W. *et al.* Peptide-labelled near-infrared quantum dots for imaging tumour vasculature in living subjects. *Nano Lett.* **6**, 669–676 (2006).
- Schipper, M. L. *et al.* A pilot toxicology study of single-walled carbon nanotubes in a small sample of mice. *Nature Nanotech.* **3**, 216–221 (2008).
- Kam, N. W., O'Connell, M., Wisdom, J. A. & Dai, H. Carbon nanotubes as multifunctional biological transporters and near-infrared agents for selective cancer cell destruction. *Proc. Natl Acad. Sci. USA* **102**, 11600–11605 (2005).
- American National Standards Institute. American national standard for the safe use of lasers. ANSI Standard Z136.1–2000 (ANSI, New York, 2000).
- Loening, A. M. & Gambhir, S. S. AMIDE: a free software tool for multimodality medical image analysis. *Mol. Imaging* **2**, 131–137 (2003).

Supplementary Information accompanies this paper at [www.nature.com/naturenanotechnology](http://www.nature.com/naturenanotechnology).

## Acknowledgements

We would like to thank J. Rosenberg for the statistical analysis. This work was supported, in part, by National Cancer Institute (NCI) Center for Cancer Nanotechnology Excellence (CCNE) U54 (to S.S.G.) and NCI In-Vivo Cancer Molecular Imaging Center (ICMIC) P50 CA114747 (to S.S.G.).

## Author contributions

A.D. built the photoacoustic instrument, designed and performed the experiments and wrote the paper. C.Z. designed, performed and analysed the Raman experiments. S.K. built the photoacoustic instrument and designed the experiments. S.V. designed and built the photoacoustic instrument. S.B. performed the experiments and helped write the paper. Z.L. synthesized the single-walled carbon nanotube conjugates.

J.L. performed the cell uptake studies. B.R.S. helped write the paper. T.M. and O.O. helped design the photoacoustic instrument. Z.C. helped perform the comparison to fluorescence imaging. X.C. provided the RGD peptides, performed the fluorescence imaging of QD-RGD conjugates and helped write the manuscript. H.D. was responsible for single-walled carbon nanotube conjugation synthesis. B.T.K. was responsible for building the photoacoustic instrument. S.S.G. was responsible for experimental design and wrote the paper.

## Author information

Reprints and permission information is available online at <http://npg.nature.com/reprintsandpermissions/>. Correspondence and requests for materials should be addressed to S.S.G.

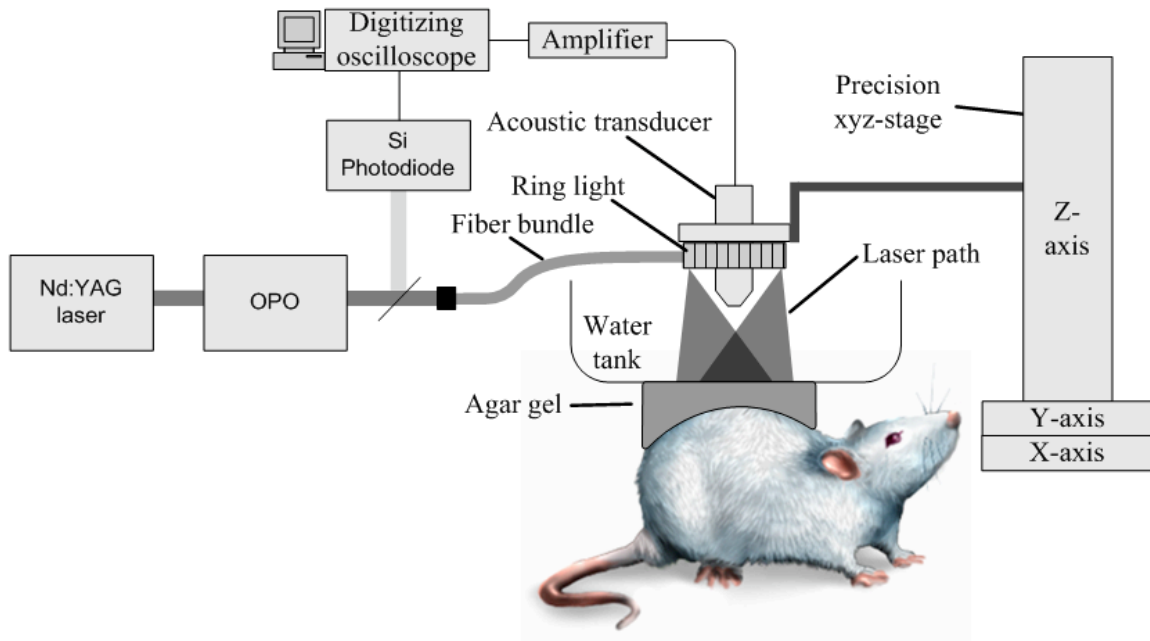
# **Carbon Nanotubes as Photoacoustic Molecular Imaging Agents in Living Mice**

Adam de la Zerda<sup>1,2</sup>, Cristina Zavaleta<sup>1</sup>, Shay Keren<sup>1</sup>, Srikant Vaithilingam<sup>2</sup>,  
Sunil Bodapati<sup>1</sup>, Zhuang Liu<sup>3</sup>, Jelena Levi<sup>1</sup>, Bryan R. Smith<sup>1</sup>, Te-Jen Ma<sup>2</sup>,  
Omer Oralkan<sup>2</sup>, Zhen Cheng<sup>1</sup>, Xiaoyuan Chen<sup>1</sup>, Hongjie Dai<sup>3</sup>, Butrus T. Khuri-Yakub<sup>2</sup>,  
Sanjiv S. Gambhir<sup>1,4</sup>

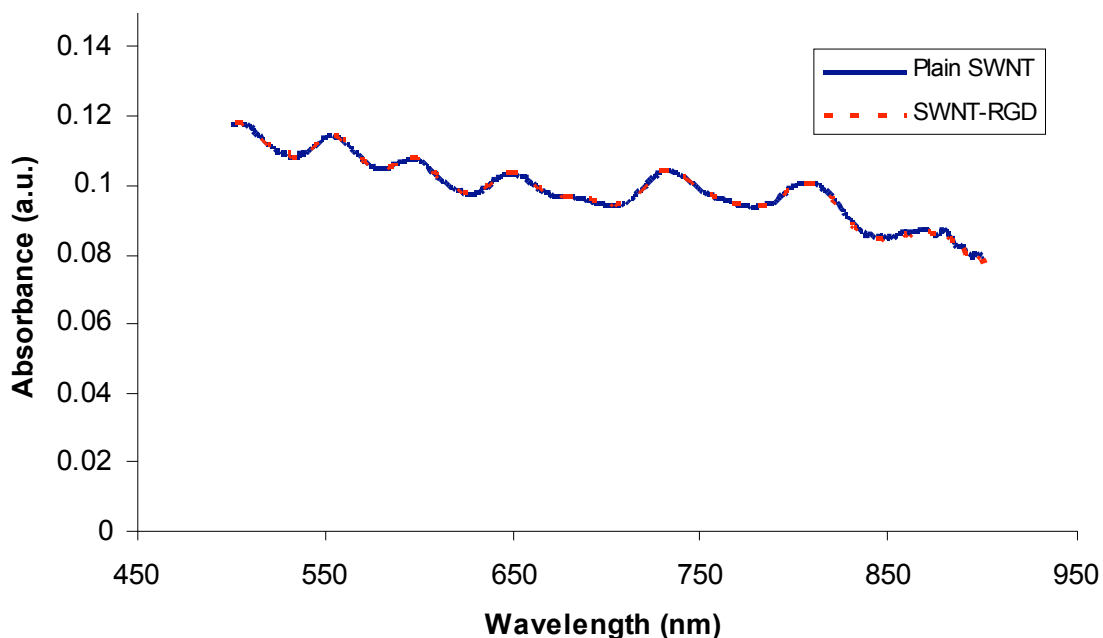
## **Supplementary Information**

<sup>1</sup>Molecular Imaging Program at Stanford, Department of Radiology and Bio-X Program, the <sup>2</sup>Department of Electrical Engineering, the <sup>3</sup>Department of Chemistry and the <sup>4</sup>Department of Bioengineering, Stanford University, Palo Alto, CA 94305, USA.  
e-mail: [sgambhir@stanford.edu](mailto:sgambhir@stanford.edu)

## Supplementary Figures



**Supplementary Figure 1 Photoacoustic imaging instrument.** A tunable pulsed laser (Nd:YAG laser and OPO) illuminated the subject through a fiber optic ring light. The photoacoustic signals produced by the sample were acquired using a 5 MHz focused transducer. A precision xyz-stage was used to move the transducer and the fiber ring along a planar 2D trajectory. The time of arrival and the intensity of the laser pulses were recorded using a silicon photodiode. This information was used to synchronize the acquisition and compensate for pulse-to-pulse variations in laser intensity. The analog photoacoustic signals were amplified using a 40 dB preamplifier and digitized using an oscilloscope.



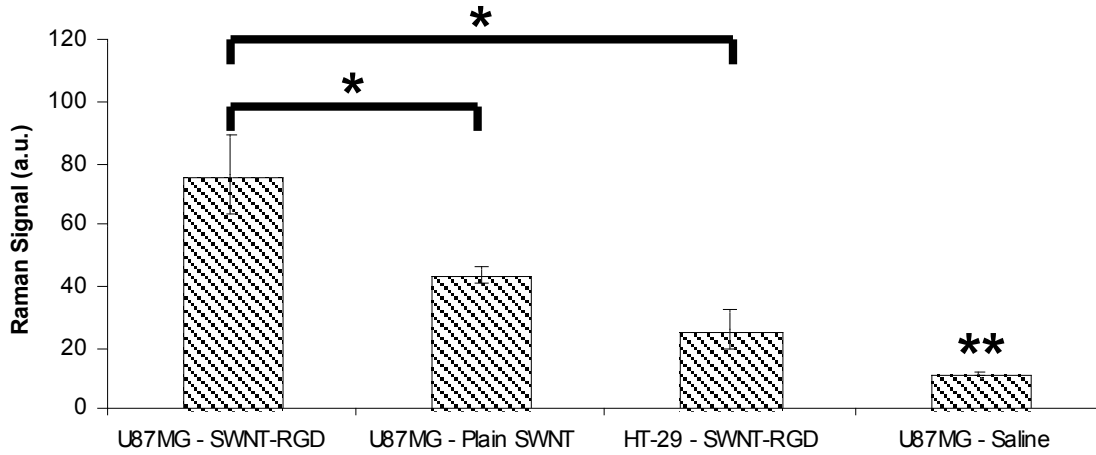
**Supplementary Figure 2 Optical absorbance of SWNTs.** The optical absorbance spectra of plain SWNTs (solid blue) and SWNT-RGD (dashed red) were measured from 500-900 nm. The spectra suggest that the RGD peptide conjugation does not perturb the optical properties of the SWNT.

### Supplementary Notes

#### **Cell uptake studies**

We exposed SWNT-RGD to U87MG cells that express  $\alpha_v\beta_3$  integrin on their surface for 30 min. Control studies included U87MG cells exposed to either plain SWNT or saline and HT-29 cells, which do not express  $\alpha_v\beta_3$  integrin on their surface, exposed to SWNT-RGD. After exposure, the cells were washed with saline to remove unbound SWNTs and scanned *ex-vivo* using a Raman microscope. SWNTs produce a very unique Raman signal<sup>1</sup>, allowing a Raman microscope to detect low concentrations of SWNTs in cells. U87MG cells that were exposed to SWNT-RGD were found to have 75% higher signal than U87MG cells exposed to plain SWNT ( $p < 0.05$ ) and 195% higher signal than HT-

29 cells exposed to SWNT-RGD ( $p < 0.05$ ). Cells exposed to saline only showed negligible signal compared to any of the groups ( $p < 0.05$ ) (**Supplementary Figure 3**).



**Supplementary Figure 3 SWNT cell uptake studies.** U87MG incubated with SWNT-RGD showed 75% higher SWNT signal than control U87MG cells which were incubated with plain SWNT and 195% higher SWNT signal than HT-29 cells which were incubated with SWNT-RGD. “ \* “ indicates  $p < 0.05$ . U87MG cells incubated with saline only showed significantly lower signal than all groups (“ \*\* “ indicates  $p < 0.05$  compared to all other groups on the graph).

### Theoretical tissue background calculation

The SWNTs used in this study had an absorbance  $A = 6.2 \cdot 10^6 \text{ cm}^{-1} \text{ M}^{-1}$  at 690 nm (measured using DU-640 spectrophotometer, Beckman Coulter). Assuming light absorption accounts for most of the absorbance of the SWNTs, we get that  $\mu_{CA}(\lambda, C) = \ln(10) \cdot A(\lambda) \cdot C$ , where  $\mu_{CA}$  and  $C$  are the contrast agent optical absorption coefficient and concentration respectively. Upon light exposure  $I$  to the absorber at wavelength  $\lambda$ , the absorber will produce a pressure wave  $P = \Gamma \cdot I \cdot \mu_a(\lambda)$ , where  $\Gamma$  is the Gruneisen coefficient and  $\mu_a(\lambda)$  is the optical absorption coefficient of the absorber. The optical absorption (and hence the background photoacoustic signal) of tissues varies between different locations in the body. This variation is due to different amounts of  $\text{HbO}_2$ , Hb and melanin that leads to different optical absorption characteristics and therefore to

different endogenous photoacoustic background signals. We conclude that typical tissues with absorption coefficient of  $0.1-1 \text{ cm}^{-1}$  will produce a background photoacoustic signal that is equivalent to the photoacoustic signal produced by 7-70 nM of SWNTs.

Importantly, in cases where background signal is mixed with the contrast agent signal (e.g., background cannot be measured prior to contrast agent administration or is not spectrally separated from the contrast agent signal), sensitivity criteria typically requires that the contrast agent signal will be greater than or equal to the tissue background signal. This requirement can be formulated as:  $P_{CA} \geq P_{Tissue}$ , where  $P_{CA}$  and  $P_{Tissue}$  are the photoacoustic pressure wave from the contrast agent and the tissue respectively. Assuming the contrast agent does not affect the Gruneisen coefficient of the tissue, this criterion reduces to:  $\mu_{CA}(\lambda) \geq \mu_{Tissue}(\lambda)$ , where  $\mu_{CA}(\lambda)$  and  $\mu_{Tissue}(\lambda)$  are the optical absorption coefficients of the contrast agent and the tissue respectively.

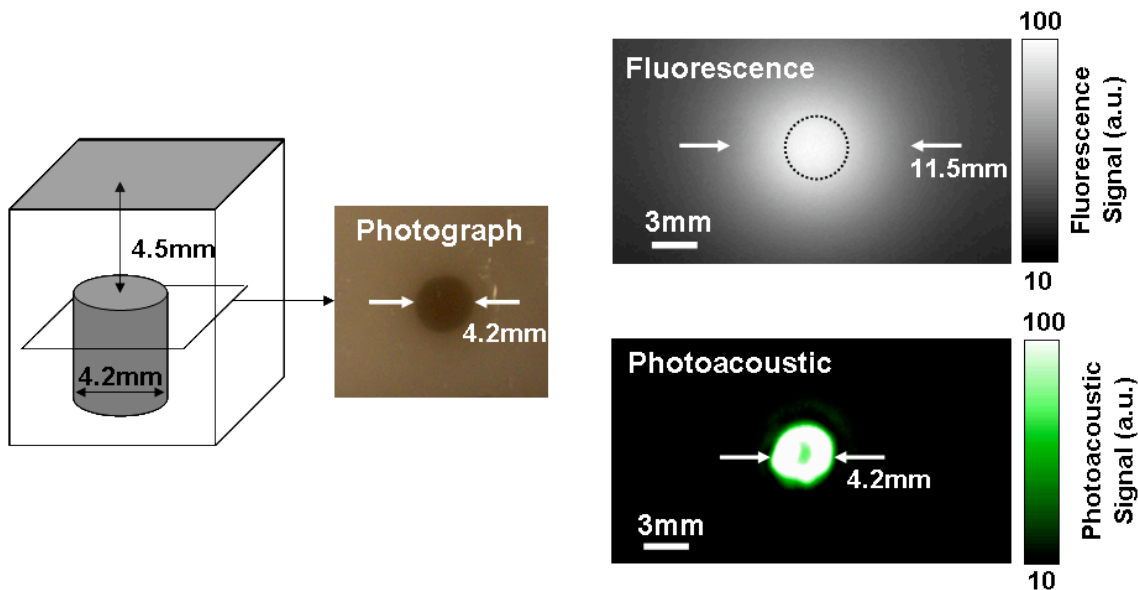
### **Calculation of percentage injected dose per gram of tissue**

We have shown that the photoacoustic signal produced by 50 nM of SWNTs is equivalent to the endogenous photoacoustic signal produced by tissues. Since mice injected with SWNT-RGD showed 67% increase in photoacoustic signal produced by tumours, the SWNTs concentration in the tumour can be estimated to be 33.5 nM. The mice were injected with 240 pmol of SWNT-RGD (200  $\mu\text{l}$  at 1.2  $\mu\text{M}$  concentration). Assuming that 1  $\text{mm}^3$  of tissue weights 1 mg, the percentage injected dose per gram of tissue (%ID/g) is therefore  $\sim 14 \text{ \%ID/g}$ .

### **Comparison to optical fluorescence imaging using quantum dots**

We show the superiority of our photoacoustic strategy by comparing it to fluorescence imaging with quantum dots (QDs). We constructed an agar-based phantom with a scattering coefficient,  $\mu_s^{-1} = 1 \text{ mm}^{-1}$ , similar to that of tissues and negligible absorption. The phantom had a cylindrical inclusion (4.2 mm in diameter) embedded 4.5 mm below the phantom surface (**Supplementary Figure 4**). The inclusion was filled with a cocktail of plain SWNT and QDs at 200 nM each. The QDs were  $\sim 30 \text{ nm}$  in diameter with emission wavelength of 800 nm. The phantom was scanned under a fluorescence imaging instrument and under our photoacoustic imaging instrument (**Supplementary Figure 4**).

Control inclusions filled with plain SWNT only or QDs only showed no fluorescence signal and no detectable photoacoustic signal respectively. This is likely due to the fact that SWNTs are non-fluorescent at 800 nm (Supplementary Ref. 2). Quantum dots, on the other hand, are highly fluorescent and therefore only minimal energy is available for heating and creating photoacoustic vibrations. The fluorescence image showed a large blurred spot at the center of the phantom, with an estimated diameter of 11.5 mm (full-width half max), whereas the photoacoustic image clearly reveals the edges of the inclusion and accurately estimates its diameter to be 4.2 mm. Furthermore, the depth of the inclusion was accurately estimated in the photoacoustic image to be  $4.5 \pm 0.1$  mm (data not shown). Depth estimation at this accuracy cannot be done using fluorescence imaging. Additionally, the signal to noise ratio (SNR), which is associated with sensitivity, was significantly higher in the photoacoustic image (SNR = 38) than in the fluorescence image (SNR = 5.3).



**Supplementary Figure 4 Comparison between photoacoustic imaging using SWNTs and fluorescence imaging using QDs.** Cylindrical inclusion filled with a mixture of SWNTs and QDs at equal concentrations was positioned 4.5 mm below the surface of a tissue mimicking phantom. Photographic image (right) of a horizontal slice through the phantom illustrates that the inclusion is 4.2 mm across. Fluorescence (top right) and photoacoustic (bottom right) images of the phantom. The dotted circle in the fluorescence

image illustrates the real location of the inclusion. The photoacoustic image represents a horizontal slice in the 3D image, 5 mm below the phantom surface. The estimated diameter of the inclusion in the fluorescence image is 11.5 mm (full-width half max) whereas the photoacoustic image accurately estimated the inclusion to be 4.2 mm across.

### **Supplementary Methods**

**Tumour *ex-vivo* analysis using Raman microscopy.** At the conclusion of every photoacoustic study (4 hr post-injection) the mice were sacrificed and the tumours were surgically removed. The tumours were then scanned using a Raman Microscope (Renishaw Inc.). The microscope has a laser operating at 785 nm with a power of 60 mW. A computer-controlled translation stage was used to create a two dimensional map of the SWNT signal in the excised tumours with 750  $\mu\text{m}$  step size using 12X open field lens. Quantification of the Raman images was performed by using the Nanoplex™ SENSERSee software (Oxonica Inc.) where the mean Raman signal detected from the tumours was calculated.

**Mouse arrangement in the photoacoustic system.** Female nude mice were used for all the photoacoustic studies. The mice scanned in the photoacoustic system were fully anesthetized using isoflurane delivered through a nose-cone. Prior to the photoacoustic scan, the areas of interest were covered with agar gel to stabilize the area and minimize any breathing and other motion artifacts. A saran-wrap water bath was placed on top of the agar gel. An ultrasonic transducer, placed in the water bath, was therefore acoustically coupled to the mouse tissues. This setup allowed the ultrasonic transducer to move freely in 3D while not applying any physical pressure on the mouse.

**Characterization of SWNT photoacoustic properties.** We prepared a gel phantom using 1% Ultrapure Agarose (Invitrogen) and 1% intra-lipid (Liposyn II 10%, Abbott Laboratories) to induce scattering into the phantom. We waited 30 min for the solution to solidify and created cylindrical wells 4.2 mm in diameter into the phantom. We then

mixed plain SWNT with warm liquid agar at ratio of 1:4 so that the final concentration of the SWNG was 200 nM and poured the solution into the wells. The same procedure was then repeated for SWNT-RGD. After the agar solidified, we covered the wells by another thin layer of warm agar and waited for 30 min for agar to solidify. A complete photoacoustic image of the phantom was acquired at wavelengths between 690-800 nm in 5 nm steps. The photoacoustic signals were compensated for laser power and photodiode response in the difference wavelengths, so that each measurement represents only the inherent photoacoustic signal produced by SWNTs. For image analysis, a 3D ROI was drawn over the SWNT in the phantom and the mean signal in the ROI was calculated.

To test the linearity of the photoacoustic signal as a function of SWNT concentration we used an agar-phantom with no scattering or absorbing additives (i.e. no intra-lipid). SWNTs at increasing concentration were mixed with warm liquid agar in ratio of 1:3 to form SWNTs solutions at 25, 50, 100, 200, 300, 400 nM. Inclusions 3 mm under the phantom surface were filled with the various SWNTs solutions (three inclusions for each concentration, 100  $\mu$ l per inclusion). A complete photoacoustic image of the phantom was acquired at 690 nm with step size of 0.5 mm. 3D cylindrical ROIs at the size of the inclusion were used to estimate the photoacoustic signal from each well.

**Photoacoustic detection of SWNTs in living mice.** Plain SWNT at 6 different concentrations were mixed with matrigel (Matrigel Basement Membrane Matrix, Phenol Red-free, Becton Dickinson) at 1:1 ratio creating plain SWNT solutions at 50, 100, 200, 300, 400 and 600 nM. The solutions were then injected subcutaneously (30  $\mu$ l) to the lower back of mouse (n = 3). After the matrigel solidified in its place (a few minutes) the back of the mouse was scanned under the photoacoustic system. Interestingly, SWNTs at concentration of 200 nM and above had a typical black color. A photoacoustic image with lateral step size of 0.5 mm was acquired using the 5 MHz transducer at 690 nm wavelength. Following the photoacoustic scan, an ultrasound image was acquired using the 25 MHz transducer and the two images were then coregistered. Quantification of the photoacoustic signal was done by drawing a 3D ROI over the inclusion volume that is

illustrated in the ultrasound image. The volume of the ROIs was kept at 30 mm<sup>3</sup> (equivalent to the 30 µl that were injected).

**Cell uptake studies.** We exposed  $1.2 \times 10^6$  U87MG cells to 100 µl of 600 nM SWNT-RGD. As a control,  $1.2 \times 10^6$  U87MG cells were exposed to same volume and concentration of plain SWNT. Another  $1.2 \times 10^6$  U87MG control group was exposed to PBS 1X (PBS pH 7.4 1X, Invitrogen). Additionally,  $1.2 \times 10^6$  cells HT-29 cells were exposed to 100 µl of 600 nM SWNT-RGD (n = 3 in all groups). The cells were exposed for 30 min, and then centrifuged at 12,400 RPM for 3 min. All excess liquid was removed and cells were washed with PBS twice. The cells were then suspended in 15 µl of liquid agar gel and were scanned using a Raman microscope.

**Comparison to optical fluorescence imaging using quantum dots.** We have prepared a gel phantom using 1% Ultrapure Agarose (Invitrogen) and 1% intra-lipid (Liposyn II 10%, Abbott Laboratories). We waited 30min for the agar-lipid solution to solidify and then created cylindrical wells with diameter of 4.2 mm in the phantom. The wells were then filled with a cocktail of QDs (Qdot(r) 800 ITK™ amino (PEG) quantum dots, Invitrogen), and plain SWNT at equal concentration. Control wells were filled with QDs only and plain SWNT only. Liquid agar was added to all wells at a ratio of 4:1 to allow the well content to solidify. After the dilution with the liquid agar, the concentration of plain SWNT and QDs in the wells was 200 nM. We waited 30 min allowing the agar to solidify and then poured a second layer, 4.5 mm in height, of warm agar-lipid liquid. We waited 30 min and then scanned the phantom in a fluorescence imaging instrument Maestro (CRI). A band pass excitation filter centered around 645 nm and a 700 nm long pass emission filter were used for the scan. The tunable band pass filter was set to scan the fluorescence emission from the phantom at wavelengths between 700 nm to 950 nm. An exposure time of 300 ms was found to maximize the fluorescence signal from the QD-SWNT well while not saturating the camera. Maestro proprietary software was used to calculate the full-width half max (FWHM). SNR was calculated as the maximal signal acquired from the well divided by the average signal in a small ROI drawn 14 mm away from the inclusion's center. We then acquired photoacoustic and ultrasound images of the

phantom. The laser wavelength was set to 690 nm and averaging of 16 laser pulses per photoacoustic a-scan was used. The lateral step size was set to 250  $\mu\text{m}$ . The resulting photoacoustic image was analyzed using AMIDE software. The estimated depth of the inclusion was determined by overlaying the photoacoustic image on the ultrasound image which shows the surface of the agar-phantom. The estimated inclusion diameter was measured directly from the photoacoustic image and the image SNR was calculated as the photoacoustic signal at the inclusion area divided by the mean signal outside the inclusion.

The synthesis of QD-RGD that were used in the fluorescence tumour targeting experiment is described elsewhere<sup>1</sup>. The mice were inoculated with  $10^7$  U87MG cells, and tumours were allowed to grow to 500  $\text{mm}^3$ . 200 pmol of QD-RGD were injected via the tail vein to the mice. The mice were imaged 6 hr post-injection using the Maestro (CRI) fluorescence imaging instrument. Excitation filter of 575-605 nm, emission long pass filter of 645 nm and liquid crystal filter range between 650 nm to 850 nm were used for this scan.

### **Supplementary References**

1. Jorio, A., Saito, R., Dresselhaus, G. & Dresselhaus, M. S. Determination of nanotubes properties by Raman spectroscopy. *Philos. Transact. A Math. Phys. Eng. Sci.* 362, 2311-36 (2004).
2. Barone, P. W., Baik, S., Heller, D. A. & Strano, M. S. Near-infrared optical sensors based on single-walled carbon nanotubes. *Nat Mater* 4, 86-92 (2005).